Comprehensive investigation of the extremely low lattice thermal conductivity and thermoelectric properties of $BaIn_2Te_4$

Tanju Gürel [1,*] Yasemin Aslantürk Altunay [1] Pınar Bulut [1] Serbülent Yıldırım [1] and Cem Sevik [2,3,†]

[1]*Department of Physics, Tekirdağ Namik Kemal University, Tekirdağ TR-59030, Turkey*

[2]*Department of Mechanical Engineering, Eskisehir Technical University, Eskisehir TR-26555, Turkey*

[3]*Department of Physics & NANOlab Center of Excellence, University of Antwerp, Groenenborgerlaan 171, B-2020 Antwerp, Belgium*

(Received 19 September 2022; revised 26 October 2022; accepted 27 October 2022; published 21 November 2022)

Recently, an extremely low lattice thermal conductivity value has been reported for the alkali-based telluride material $BaIn_2Te_4$. The value is comparable with low-thermal conductivity metal chalcogenides, and the glass limit is highly intriguing. Therefore, to shed light on this issue, we performed first-principles phonon thermal transport calculations. We predicted highly anisotropic lattice thermal conductivity along different directions via the solution of the linearized phonon Boltzmann transport equation. More importantly, we determined several different factors as the main sources of the predicted ultralow lattice thermal conductivity of this crystal, such as the strong interactions between low-frequency optical phonons and acoustic phonons, small phonon group velocities, and lattice anharmonicity indicated by large negative mode Grüneisen parameters. Along with thermal transport calculations, we also investigated the electronic transport properties by accurately calculating the scattering mechanisms, namely the acoustic deformation potential, ionized impurity, and polar optical scatterings. The inclusion of spin-orbit coupling (SOC) for electronic structure is found to strongly affect the *p*-type Seebeck coefficients. Finally, we calculated the thermoelectric properties accurately, and the optimal ZT value of *p*-type doping, which originated from high Seebeck coefficients, was predicted to exceed unity after 700 K and have a direction averaged value of 1.63 (1.76 in the *y*-direction) at 1000 K around 2×10^{20} cm^{-3} hole concentration. For *n*-type doping, a ZT around 3.2×10^{19} cm^{-3} concentration was predicted to be a direction-averaged value of 1.40 (1.76 in the *z*-direction) at 1000 K, mostly originating from its high electron mobility. With the experimental evidence of high thermal stability, we showed that the $BaIn_2Te_4$ compound has the potential to be a promising mid- to high-temperature thermoelectric material for both *p*-type and *n*-type systems with appropriate doping.

DOI: 10.1103/PhysRevB.106.195204

I. INTRODUCTION

For many years, tellurium-based thermoelectric materials have been studied extensively due to their high Seebeck coefficients, low thermal conductivity, and the resulting high figure of merit. Among these materials, Bi_2Te_3 [1] and PbTe [2,3] are the most well known due to their good thermoelectric performance. Based on this potential, many ternary telluride materials, such as chalcopyrites [4–7], thallium-based materials [8–11], and other complex materials [12–14], have also been studied for their thermoelectric properties. Also, complex thermoelectric materials [15], which are known to have a large number of atoms and atomic species in their unit cells with low symmetry and which usually exhibit low thermal conductivity, have been considered. Skutterudites [16,17], clathrates [18], and Zintl phases [19,20] are well-known families of these types of materials that satisfy the optimum balance for thermoelectric materials—the phonon-glass electron-crystal concept [21], where the electrons of a thermoelectric material are expected to behave like metals, and the phonons (vibrational modes) behave like glasses.

To satisfy the optimum balance in the bulk materials scale, the alkali-based AB_2Te_4 (A = Mg,Ca,Sr,Ba and B = Al,Ga,In) family, as a specific class of telluride compounds, has been synthesized for decades [22–28] and has become an emerging class of materials due to their potential in thermoelectric applications [25–27,29]. For some of these tellurides possessing diverse crystal structures such as cubic [29], tetragonal [22–24], orthorhombic [25,27,28], and triclinic crystal structures [23], promising results have been reported.

Recently, Ishtiyak *et al.* [27] reported experimentally that orthorhombic $BaIn_2Te_4$ exhibits thermal conductivity as low as 0.30 W/mK at 965 K. Intriguingly, this value, which is comparable with low-thermal conductivity metal chalcogenides and the glass limit, is one of the lowest values reported for this class of materials [25,26]. The thermoelectric properties of the undoped polycrystalline samples of $BaIn_2Te_4$ material were also investigated experimentally in the same study. Despite the predicted extremely low lattice thermal conductivity, the thermoelectric performance of this material was measured as being quite low, with $ZT = 0.06$ at 965 K. However, the measured low value was attributed not to the potential of the material but to the very low intrinsic doping

*Corresponding author: tgurel@nku.edu.tr

†cem.sevik@uantwerpen.be

(carrier concentration) of the prepared samples. Strategies such as spark plasma sintering and chemical doping were proposed to improve the corresponding thermoelectric efficiency. Therefore, it is worth predicting the potential of this material as thermoelectric prior to further experimental investigations.

On the other hand, $BaIn_2Te_4$, having 14 atoms in its primitive cell, is a semiconducting alkali telluride with orthorhombic *Cccm* structure, and it has one-dimensional (1D) chains of distorted tetrahedrons. These tetrahedrons contain indium atoms surrounded by tellurium atoms, and they reside together with weakly bonded barium atoms in a cagelike framework. The central indium atoms align in a distorted zigzag structure and result in a notable effect on both electron and phonon transport [30–32]. In that sense, the transport and thermoelectric properties of these materials are anisotropic, and highly accurate approaches require an investigation of direction-dependent transport properties.

Therefore, in this study, using phonon Boltzmann transport and electron-phonon coupling approaches based on first-principles calculations, we investigated the thermal and electronic transport properties of $BaIn_2Te_4$. We found that calculated thermal conductivity is in perfect agreement with the experiment. Together with large Seebeck coefficients of hole-doping (*p*-type), we predicted considerably high performance with an average ZT value, 1.63 at 1000 K. The mobility of electron-doping (*n*-type) was found to be much larger than that of hole-doping, and the average ZT for that case was calculated as 1.40 at 1000 K.

II. COMPUTATIONAL DETAILS

All the first-principles calculations were performed using the Vienna Ab-initio Simulation Package (VASP) [33], which is based on density functional theory [34,35] in the framework of the plane-wave pseudopotential method. The interactions between ions and electrons were described with projector augmented wave (PAW) pseudopotentials [36], considering the Ba 5*s* 5*p* 6*s*, In 4*d*, 5*s*, 5*p*, and Te 5*s*, 5*p* states as valence states. Perdew-Burke-Ernzerhof (PBE) [37] parametrization was adopted for the exchange and correlation functional, which is based on the generalized gradient approximation (GGA). We have also included spin-orbit coupling interaction in the structural and electronic structure calculations, and its effects on the electronic and thermoelectric properties were compared with the pure GGA-PBE results. To obtain a more reliable estimation of the band gap, a Heyd-Scuseria-Ernzerhof (HSE06) [38] -type hybrid functional was used.

An energy cutoff value of 400 eV was found to be converged for plane waves, and a convergence criterion of 10^{-7} eV was taken for self-consistent-field calculations. In the geometric optimization calculations, the residual forces acting on each atom were relaxed with a criterion of 10^{-4} eV/Å. For the total energy and geometric optimization calculations, a converged $6 \times 6 \times 3$ *k*-grid was used and a denser $12 \times 12 \times 6$ grid was chosen for the subsequent calculations of the electronic density of states and thermoelectric coefficients.

Second-order interatomic force constants (IFCs) and subsequently the phonon dispersion curves and the phonon density of states were obtained within the supercell finite-difference method as implemented in PHONOPY code [39]. We used $2 \times 2 \times 2$ supercells and a $3 \times 3 \times 2$ *k*-point grid for second-order IFCs. Third-order force constants were calculated with thirdorder.py script [40], which also uses the finite-difference method. In these calculations, a $3 \times 3 \times 2$ supercell as cell size, a single Γ-centered *k*-point as reciprocal space grid, fourth nearest neighbors as a maximum atomic interaction distance, and 0.01 Å as displacement of atomic perturbations were considered.

Phonon transport properties were obtained with SHENGBTE [40] code, which solves linearized phonon Boltzmann transport equations (BTEs). Apart from phonon-phonon scatterings, the phonon-isotope scattering from the naturally occurring isotope concentrations were also included. In the SHENGBTE calculations, for the *q*-grid convergence, calculations were performed for the scalebroad [40] parameters 1.0 and 0.1 on a $12 \times 12 \times 9$ grid. The final calculations were performed with the value scalebroad = 0.1 on a $16 \times 16 \times 12$ *q*-grid, resulting in ∼2% difference in convergence calculations.

Electron transport properties such as electrical conductivity, electronic thermal conductivity, and Seebeck coefficients have been calculated in the framework of AMSET [41] code, which uses the momentum relaxation-time approximation (MRTA) in order to calculate scattering rates and mobilities within the Born approximation. In the AMSET code, relaxation times are estimated by a number of different band and *k*-point-dependent scattering processes instead of a constant relaxation-time approach as implemented in the widely used BOLTZTRAP code [42,43]. Among these processes, acoustic deformation potential (ADP) scattering is responsible for acoustic phonon-electron interactions. Ionized impurity scattering (IMP) represents the scattering of charge carriers by ionization of the lattice. Interactions between polar optical phonons and electrons are termed polar optical scattering (POP). One other scattering mechanism also implemented in AMSET code is piezoelectric scattering (PIE), which considers the coupling between acoustic waves and charge carriers induced by macroscopic electric fields created by elastic strain. We omit piezoelectric scattering in our calculations because the $BaIn_2Te_4$ material belongs to the centrosymmetric *Cccm* space group [27] and the piezoelectric moduli vanish. The resulting electronic relaxation times (τ) (the inverse of scattering rates) of the considered scattering processes can be written by following Matthiessen's rule:

$$\frac{1}{\tau} = \frac{1}{\tau^{\mathrm{ADP}}} + \frac{1}{\tau^{\mathrm{IMP}}} + \frac{1}{\tau^{\mathrm{POP}}} + \frac{1}{\tau^{\mathrm{PIE}}}. \tag{1}$$

The ADP, IMP, and PIE scatterings are described as elastic scattering, where electrons do not gain or lose energy in these type of scattering processes. For the POP-type processes, inelastic scattering occurs because of a phonon emission or absorption. The AMSET code uses the momentum relaxation-time approximation for elastic scatterings, and the self-energy relaxation-time approximation for inelastic scatterings.

The scattering rates for the elastic scatterings from an initial $n\mathbf{k}$ state to an $m\mathbf{k}+\mathbf{q}$ final state can be written using the Fermi golden rule [41]:

$$\tau^{-1}_{n\mathbf{k}\to m\mathbf{k}+\mathbf{q}} = \frac{2\pi}{\hbar}|g_{nm}(\mathbf{k},\mathbf{q})|^2\delta(\varepsilon_{n\mathbf{k}} - \varepsilon_{m\mathbf{k}+\mathbf{q}}), \tag{2}$$

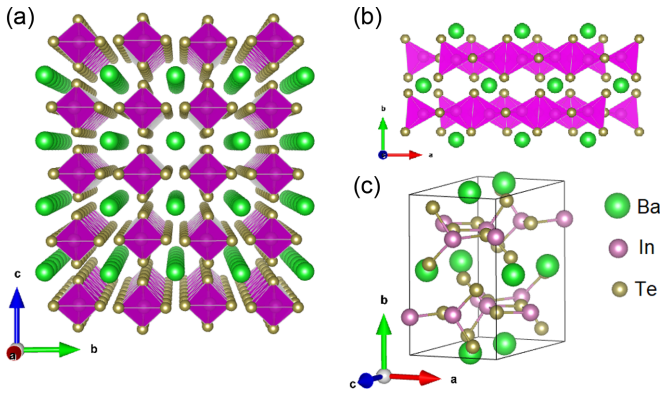

FIG. 1. Schematic view of orthorhombic $BaIn_2Te_4$ compound. (a) View in the *yz*-plane, (b) view in the *xy*-plane, and (c) the primitive cell. VESTA software [47] is used for visualization.

and for the inelastic scattering rate a similar type of equation is given as

$$\tau^{-1}_{n\mathbf{k}\to m\mathbf{k}+\mathbf{q}} = \frac{2\pi}{\hbar}|g_{nm}(\mathbf{k},\mathbf{q})|^2 \times \left[\left(n_\mathbf{q}+1-f^0_{m\mathbf{k}+\mathbf{q}}\right)\delta\left(\Delta\varepsilon^{nm}_{\mathbf{k},\mathbf{q}}-\hbar\omega_\mathbf{q}\right) + \left(n_\mathbf{q}+f^0_{m\mathbf{k}+\mathbf{q}}\right)\delta\left(\Delta\varepsilon^{nm}_{\mathbf{k},\mathbf{q}}+\hbar\omega_\mathbf{q}\right)\right], \quad (3)$$

where $\hbar$ is the reduced Planck constant, δ is the Dirac delta function, $\varepsilon_{n\mathbf{k}}$ is the energy of the $|n\mathbf{k}\rangle$ state, n is the Bose-Einstein distribution, f is the Fermi-Dirac distribution, and the terms $-\hbar\omega_\mathbf{q}$ and $\hbar\omega_\mathbf{q}$ correspond to the phonon emission and absorption, respectively. The term $g_{nm}(\mathbf{k},\mathbf{q})$ is the coupling matrix element of the considered scattering mechanism, and the detailed forms of all the scattering matrix elements are given in Ref. [41].

To obtain the scattering rates, all the required material parameters, such as dense uniform band structures, wave-function coefficients, elastic constants, deformation potentials, static and high-frequency dielectric constants, and polar-phonon frequency were calculated from DFT and density functional perturbation theory (DFPT) [44]. Details of the calculated parameters are given in Table S1 of the Supplemental Material [45]. The subsequent transport properties, such as the Seebeck coefficient, electrical conductivity, and electronic thermal conductivity, were calculated from the Onsager transport coefficients [42,43]. During the AMSET calculations, a converged interpolation factor of 20 was used for the GGA-PBE scheme, which corresponds to a $49 \times 49 \times 25$ grid. For GGA-PBE-SOC, we have used a converged interpolation factor of 10 with a $53 \times 53 \times 27$ grid.

III. RESULTS

A. Structural properties

The $BaIn_2Te_4$ compound crystallizes in an orthorhombic lattice structure having the space group $D^{20}_{2h} - Cccm$ (sp. gr. no. 66). The schematic representation of the structure is given in Fig. 1. There exist 14 atoms in the primitive cell [Fig. 1(c)] as it is twofold according to the formula unit, where two of these atoms are barium, four are indium, and eight are tellurium atoms. The basis vectors [46] of $BaIn_2Te_4$ in reduced coordinates are given in Table S2 of the Supplemental Material [45]. As shown in Figs. 1(a) and 1(b), which are visualized by VESTA [47], indium atoms that are surrounded by four tellurium atoms compose tetrahedrals and form a 1D-like chain along the *a*-axis (*x*-direction).

TABLE I. The GGA-PBE and GGA-PBE-SOC calculated lattice parameters, internal parameters, bulk modulus, and pressure derivative of bulk modulus compared with the available experimental results.

Parameter	GGA-PBE	GGA-PBE-SOC	Expt. (Ref. [27])
a (Å)	7.2598	7.2704	7.1417
b (Å)	12.314	12.312	12.034
c (Å)	12.445	12.443	12.107
z_2	0.82288	0.82263	0.82141
x_3	0.00196	0.00200	0.00156
y_3	0.26370	0.26372	0.26082
x_4	0.72792	0.72789	0.73918
y_4	0.42687	0.42707	0.42835
B_0 (GPa)	18.67	18.45	
B'_0	4.45	4.46	

In Table I, equilibrium lattice parameters, internal parameters, bulk modulus, and the pressure dependence of the bulk modulus calculated with GGA-PBE and GGA-PBE-SOC are given along with available experimental results. As seen in Table I, the GGA-PBE and GGA-PBE-SOC results are very similar and the calculated equilibrium lattice parameters are larger than the experimental values with the typical overestimation of the GGA. The calculated internal parameters are in good agreement with the experimentally reported x-ray diffraction measurements [27].

The bulk modulus and its pressure derivative are obtained by fitting the Birch-Murnaghan equation of state [48] (see the Supplemental Material [45]). The results are also shown in Table I. To the best of our knowledge, there is no experimental or theoretical bulk modulus value in the literature for $BaIn_2Te_4$. The obtained bulk modulus $B = 18.45$ GPa is a relatively low value that was also reported in some other barium-containing materials [49,50]. The pressure dependence of the bulk modulus $B'_0 = 4.46$ has been calculated, and this value is typically found in the great majority of crystals.

B. Phonon properties and lattice thermal conductivity

For a deep understanding of lattice thermal conductivity, a detailed analysis of the vibrational and phonon transport properties is required. In this section, the extremely low thermal conductivity behavior of $BaIn_2Te_4$ will be explored by examining the phonon dispersion relations, phonon density of states, and phonon transport properties such as phonon group velocities, mode Grüneisen parameters, and scattering rates.

The lattice thermal conductivity at temperature T is given as

$$\kappa_{\alpha\beta} = \frac{1}{k_B T^2 \Omega N}\sum_\lambda f_0(f_0+1)(\hbar\omega_\lambda)^2 v^\alpha_\lambda F^\beta_\lambda, \quad (4)$$

where α and β are the Cartesian coordinates, k_B is the Boltzmann constant, Ω is the unit cell volume, N is the number

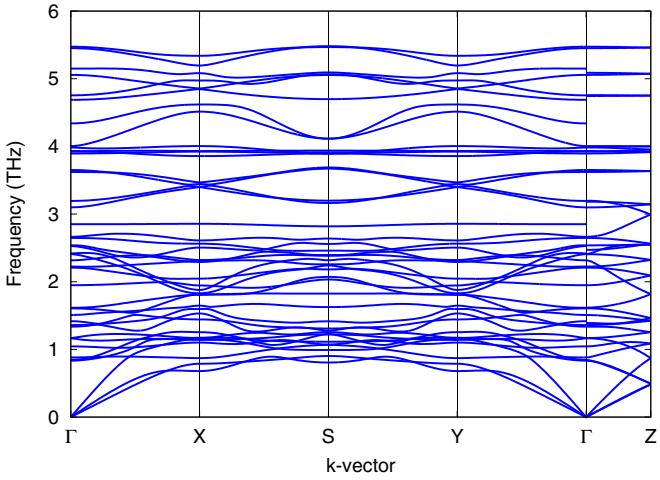

FIG. 2. Phonon dispersion relations of $BaIn_2Te_4$.

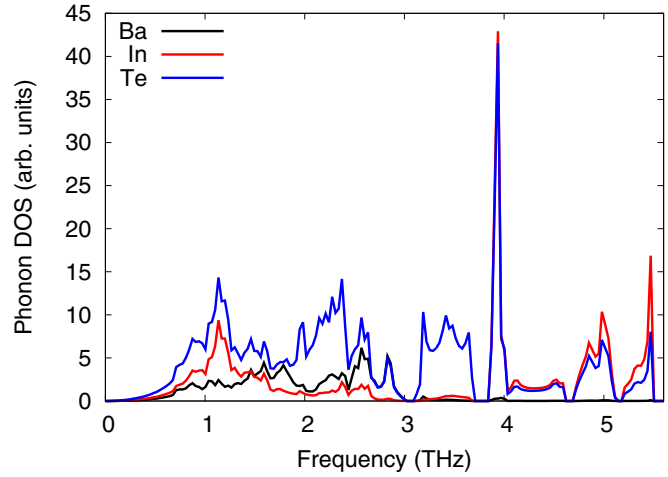

FIG. 3. Total and partial phonon density of states of $BaIn_2Te_4$.

of unit cells, f_0 is the equilibrium Bose-Einstein distribution function, ω_λ is the phonon frequency of the mode λ (representing the phonon branch index and wave number), and v_λ is the phonon group velocity. Here, F_λ is expressed as $F_\lambda = \tau_\lambda^0(v_\lambda + \Delta_\lambda)$, where τ_λ^0 is the phonon relaxation time and Δ_λ is the correction term [40]. In the relaxation-time approximation (RTA), Δ_λ is set to be equal to zero. On the other hand, taking into account the evaluation of Eq. (4), F_λ is solved iteratively from the linearized phonon Boltzmann transport equation as implemented in the SHENGBTE code [40].

Phonon dispersion relations of $BaIn_2Te_4$, calculated by solving the dynamical matrix that was obtained from second-order force constants, are shown in Fig. 2 along the high-symmetry directions of Γ-*X*-*S*-*Y*-Γ-*Z* of the Brillouin zone, including the LO/TO splitting. Since there exist 14 atoms in the primitive cell of the $BaIn_2Te_4$ material, there are a total of 42 phonon modes for each **q**-point, where three of them are acoustic modes and the remaining 39 modes are optical modes. As shown in Fig. 2, the entire phonon spectrum of $BaIn_2Te_4$ has positive frequencies in all directions, indicating a dynamically stable phase.

It is useful to note that acoustic branches have mostly low-frequency values smaller than <1 THz. The flat acoustic branches in most of the directions result in low phonon group velocities and indicate low lattice thermal conductivity. In addition, low optical modes and LA acoustic modes strongly hybridize around the 1 THz frequency region. This hybridization would provide more channels for phonon scattering, and it strongly suggests low lattice thermal conductivity. Although the dispersion of the majority of optical modes is flat, significant branches are noticeably dispersive in many frequency domains. Because the aforementioned high-branch optical modes have high group velocities, they are expected to make significant contributions to the lattice thermal conductivity.

To determine the contributions of particular atoms to the phonon spectrum, we calculated the atom-projected phonon density of states and presented the results in Fig. 3. As can be seen from the figure, tellurium atoms contribute in all frequency domains. The contribution of barium atoms, which is the heaviest atom in the $BaIn_2Te_4$ material, is only in the 0–3 THz region, and the contribution of indium atoms is mostly between the 1–2 and 4–6 THz frequency regions. Since the masses of In and Te atoms are very close to each other, we encounter strong degeneracy between two atoms. These degeneracies occur both in the high optical region (>3.8 THz) and in the acoustic low optical region (around 1 THz region).

The temperature dependence of lattice thermal conductivity calculated from Eq. (4) is shown in Fig. 4 along the *x*-, *y*-, and *z*-directions. For all temperatures, the lattice thermal conductivity in the *x*-direction (which is comprised of 1D chains) is found to be about 1.7 and 1.8 times larger compared to the *y*- and *z*-directions, respectively. Figure 4 also shows the total thermal conductivity ($\kappa_{\text{total}} = \kappa_l + \kappa_e$) reported by Ishtiyak *et al.* [27]. Because the electronic conductivity is negligibly low compared to the lattice thermal conductivity in many (undoped) semiconductor materials, we can directly compare the calculated κ_l values with the experimental result. As seen from the figure, the calculated average lattice thermal conductivity is very close to the experimental values.

To present our understanding of the mechanisms underlying the low thermal conductivity behavior of $BaIn_2Te_4$,

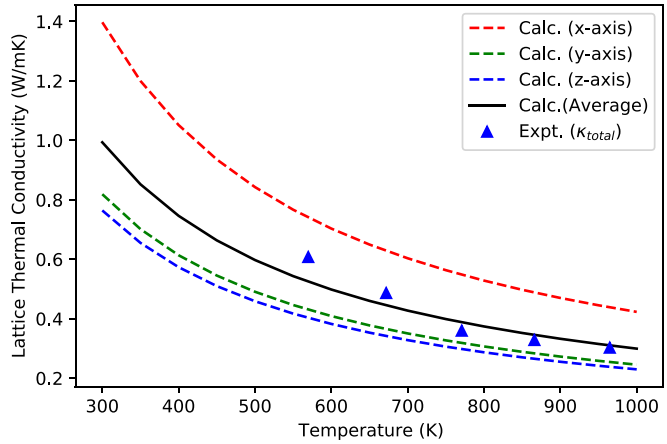

FIG. 4. Lattice thermal conductivity of $BaIn_2Te_4$ along the *x*, *y*, and *z* directions together with the average value. The experimental measurement is taken from Ref. [27].

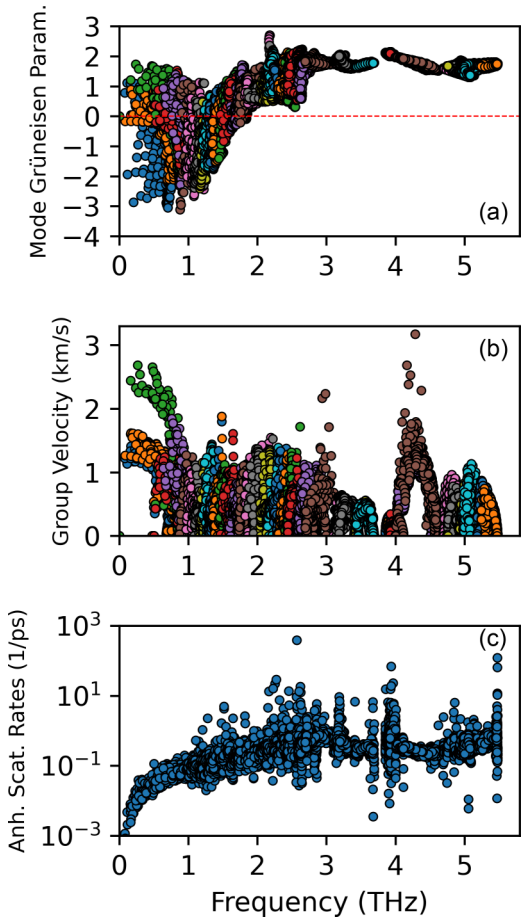

FIG. 5. The calculated (a) mode Grüneisen parameters, (b) phonon group velocities, and (c) anharmonic scattering rates of $BaIn_2Te_4$.

mode Grüneisen parameters, phonon group velocities, and anharmonic scattering rates are shown in Figs. 5(a), 5(b) and 5(c), respectively. Anharmonicity of a periodic crystal can be partially characterized by the mode Grüneisen parameters. Indeed, a large Grüneisen parameter usually points out a strong anharmonicity. As seen in Fig. 5(a), the predicted large negative Grüneisen parameters, up to a value of −3, for some acoustic modes and low-frequency (<2 THz) optical modes are parallel with this statement and indicate a strong anharmonicity of phonons in $BaIn_2Te_4$.

Figure 5(b) shows the phonon group velocities of $BaIn_2Te_4$ as a function of frequency. In the acoustic region, values up to 3 km/s corresponds to LA modes only, and group velocities of TA modes do not exceed 1.5 km/s. The low TA group velocities and hence sound velocities lead to soft elastic moduli (see Table S1 of the Supplemental Material [45]) and low bulk modulus (Table I). As a trend, optical modes are expected to have lower group velocities than acoustic modes, and their effect on thermal conductivity involves much less contribution. The phonon group velocities of optical modes mostly do not exceed 1–1.2 km/s, but it was found that the group velocities of the highly dispersed optical modes around the 3 and 4.5 THz regions are higher than the other optical modes. These high group velocities make a small contribution to the lattice

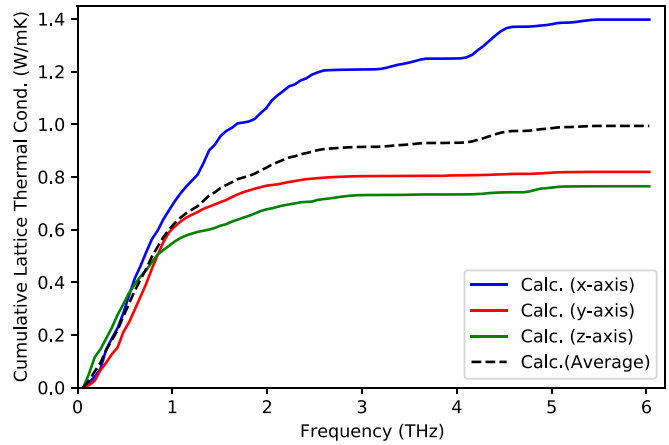

FIG. 6. The cumulative lattice thermal conductivity calculated at 300 K for $BaIn_2Te_4$ along the x-, y-, and z-directions together with the average value.

thermal conductivity, particularly in the x-direction (Fig. 6), as discussed below. The phonon group velocities of $BaIn_2Te_4$ are found to be significantly lower than the group velocities of the thermoelectric PbTe material [51], which is well known for having low thermal conductivity. Thus, it is clear that low group velocities play a significant role in understanding the low lattice thermal conductivity of $BaIn_2Te_4$.

Another important factor affecting the lattice thermal conductivity is the anharmonic scattering rates, and the calculated values at 300 K are shown in Fig. 5(c) as a function of frequency. Low anharmonic scattering rates reflect larger relaxation times and greatly increase the lattice thermal conductivity, and as can be seen from the figure, the smallest values are in the 0–1 THz acoustic region. High-frequency optical phonons mostly exhibit large scattering rates compared to acoustic modes. Nevertheless, some scattering rate values in the optical region (particularly around 4 THz) are also quite low, which cause a notable increment in the lattice thermal conductivity.

The cumulative lattice thermal conductivity is another useful quantity that manifests in the contribution of phonons with different frequencies to the total thermal conductivity. Figure 6 shows the cumulative lattice thermal conductivity as a function of the phonon frequency at room temperature (300 K). As can be seen from the figure, almost all of the contributions to the average lattice thermal conductivity come from the 0–2 THz frequency region, while the contribution from the 0–1 THz region is around 60%. The major contribution of the optical regions comes from the x-direction (the 1D-chain direction), while contributions in the y- and z-directions are very small.

C. Electronic properties

Using the GGA and GGA + SOC optimized structures, the electronic band structure of $BaIn_2Te_4$ in the frameworks of GGA-PBE and GGA-PBE-SOC was calculated along the high-symmetry directions of the Brillouin zone of the orthorhombic lattice. In addition, the HSE06 hybrid functional correction was applied to correct the failure of GGA-PBE in

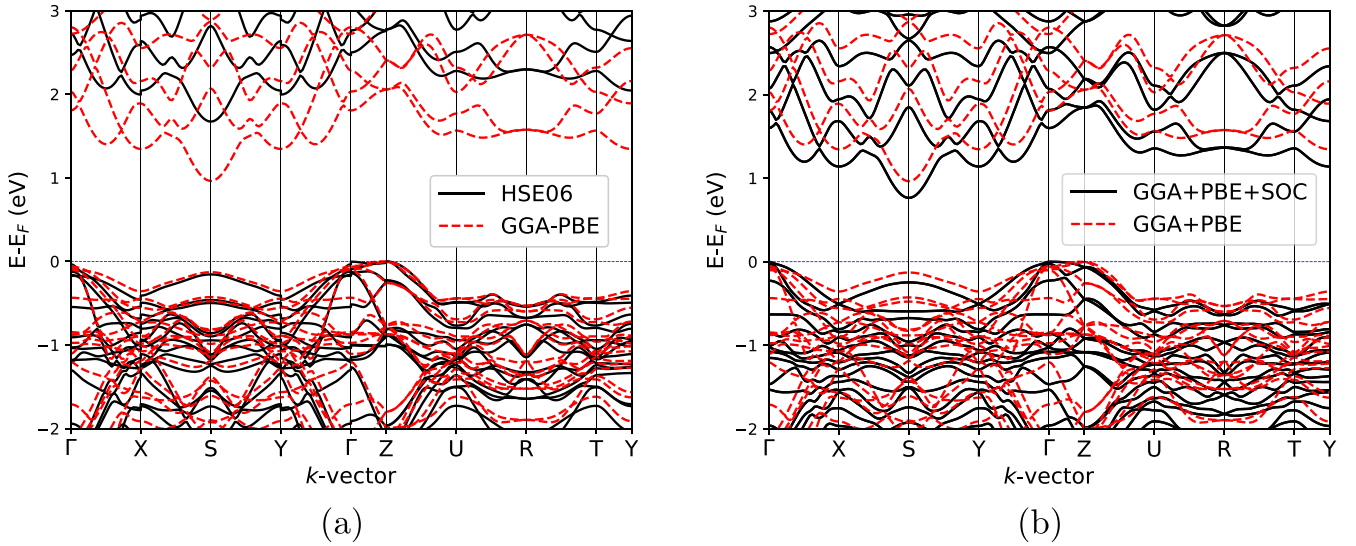

FIG. 7. Electronic band structure of $BaIn_2Te_4$ calculated with (a) HSE06 (full lines) and GGA-PBE (dashed lines), and (b) GGA-PBE-SOC (full lines) and GGA-PBE (dashed lines). The Fermi level is set to 0 eV.

determination of the band gap of semiconductor systems. The obtained results are displayed in Fig. 7. The valence-band maximum is located at the Z point, and the conduction-band minimum is located at the S point, resulting an indirect-band-gap (S-Z) values of 0.963 and 1.670 eV for GGA-PBE and HSE06, respectively [Fig. 7(a)]. For the GGA-PBE-SOC case, the valence-band maximum is located at the Γ point with a lower indirect band gap 0.76 eV [Fig. 7(b)]. The direct band gap at the Γ high-symmetry point is predicted as about 1.85 eV for GGA-PBE and 2.5 eV for HSE06. The direct band gap of the GGA-PBE-SOC calculation is found to be 1.6 eV. To the best of our knowledge, the only experimental determination of the band gap was performed in the study of Ishiyak *et al.* [27] for a polycrystalline sample of $BaIn_2Te_4$. In their optical absorption study at room temperature, they estimated the indirect- and direct-band-gap values as 0.83 eV (or lower) and 1.36 eV, respectively. These values are quite small when compared to our calculations. They stated that the obtained values remained within the limits of the spectrophotometer they used. In fact, our calculations point out that the experimental limitations might have a significant influence on reported values. Therefore, further complementary experimental electronic structure studies are required in this regard.

One important behavior of the band structure of $BaIn_2Te_4$ is having a close valence extremum of Γ, Z, and S points including twofold or threefold band degeneracy containing heavy bands. These are an indication of intrinsically large Seebeck coefficients, which leads to the higher power factor of the material [52]. By considering that the bands of GGA-PBE and HSE06 do not change too much except for the band gap, for the subsequent calculations we have used the GGA-PBE and GGA-PBE-SOC methods and applied a scissor operator to the band gap in the sense of a rigid band approximation. We set the band gap to the HSE06 value for electron transport calculations.

The calculated GGA-PBE and GGA-PBE-SOC partial and total density of states (DOS) of orthorhombic $BaIn_2Te_4$ is shown in Fig. 8. The valence band near the Fermi level is formed mainly by Te-5p orbitals together with minor contributions from Ba-4d and Ba-5p states, and the conduction band is composed of the In-5s and Ba-4d orbitals. The In atoms only appear in the conduction band, and they make no obvious contribution to the valence states. It may be expected that the p-type doping and alloying on In sites would minimally affect the valence-band structure and hence the mobility, which are very important for thermoelectric performance. The large

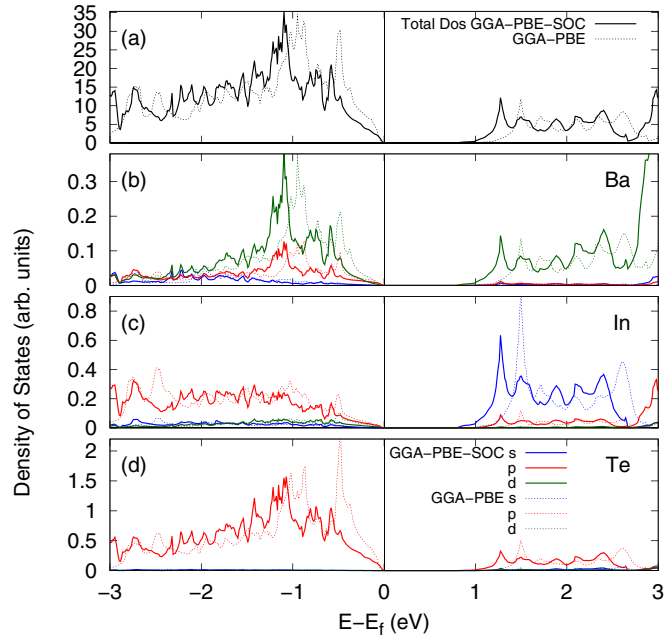

FIG. 8. Electronic density of states of $BaIn_2Te_4$ calculated with GGA-PBE-SOC (full lines) and GGA-PBE (dotted lines). (a) Total density of states and partial density of states of atoms (b) barium, (c) indium, and (d) tellurium. The Fermi level is set to 0 eV.

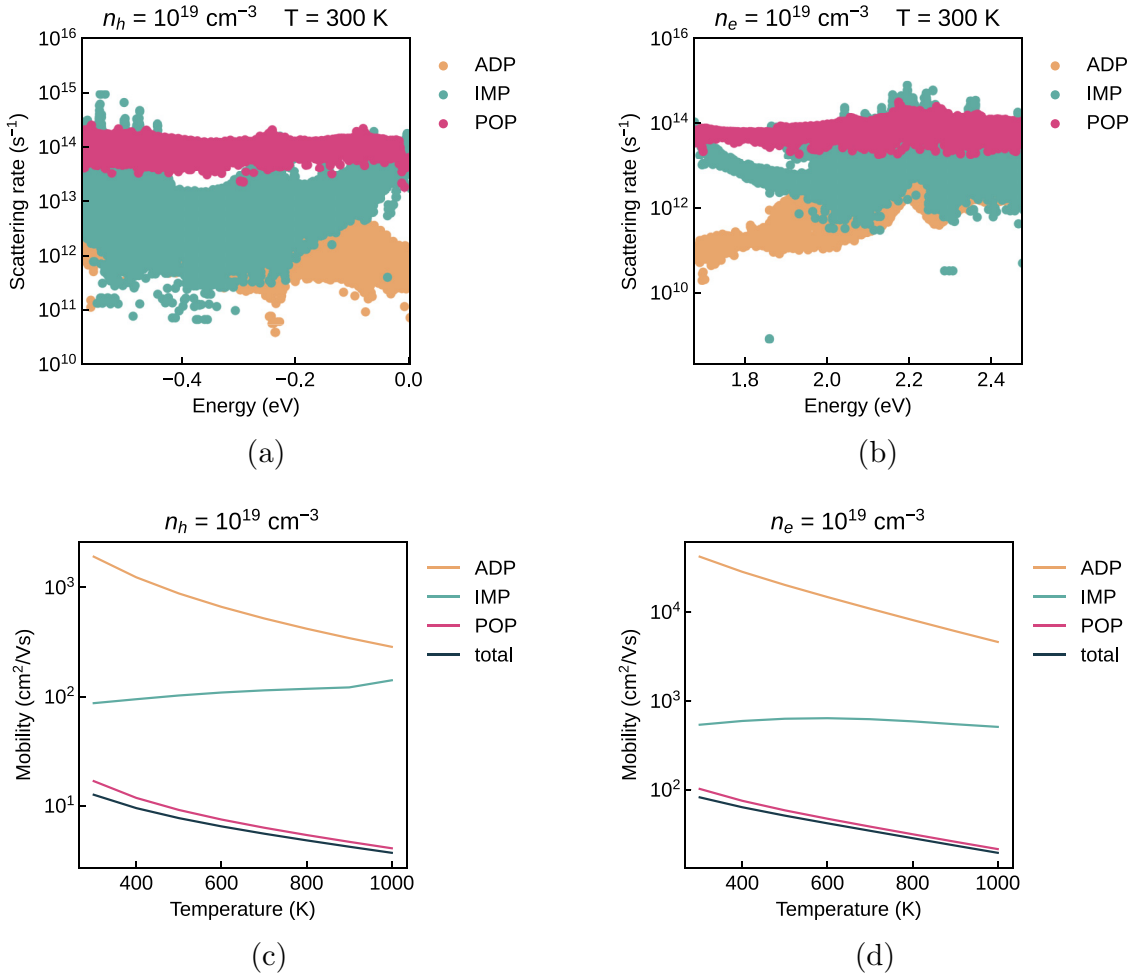

FIG. 9. The total and scattering mechanism resolved room-temperature electronic scattering rates for (a) hole doping and (b) electron doping calculated with GGA-PBE-SOC. The total and scattering mechanism resolved mobility as a function of temperature for (c) hole doping and (d) electron doping. All the results are given at 10^{19} cm^{-3} carrier concentration.

slope of the total DOS [Fig. 8(a)] in the valence band near Fermi level also suggests large Seebeck coefficients together with the possible use of $BaIn_2Te_4$ as a *p*-type thermoelectric material. As shown in the figure, the GGA-PBE-SOC results meaningfully lower this slope compared to GGA-PBE, which is an indication that the spin-orbit interactions cannot be neglected.

D. Thermoelectric properties

Before discussing the thermoelectric properties, it is convenient to investigate carrier scattering rates and mobility, where the GGA-PBE-SOC results are given in Fig. 9 at 300 K with a 10^{19} cm^{-3} carrier concentration. The calculated scattering rates as a function of energy are shown in Figs. 9(a) and 9(b) for *p*-type (hole doping) and *n*-type (electron doping), respectively. It is clearly seen that polar-optical scattering rates have the highest values followed by the impurity scattering. ADP scatterings have the lowest values, particularly at energies through the band edges. Figures 9(c) and 9(d) present the total and scattering type resolved mobilities with respect to temperature for *p*-type and *n*-type doping, respectively. We have found that the POP scattering is the dominant scattering for both doping types. This behavior was also found in many well-known thermoelectric materials, e.g., PbTe [53], SnS [54], and SnSe [55], and in many complex materials [32,56–59]. Total, POP, and ADP mobility decrease with increasing temperature, and the IMP scattering is almost independent of temperature.

Figure 10 presents the calculated Seebeck coefficients, electrical conductivity, and electronic thermal conductivity with respect to carrier concentration for both *p*-type and *n*-type doping. Both GGA-PBE and GGA-PBE-SOC calculations are presented for comparison. All results are given as the average of the *x*-, *y*-, and *z*-directions. The direction-oriented results can be found in Fig. S1 of the Supplemental Material [45]. For both types of doping, the Seebeck coefficients increase with temperature and decrease with carrier concentration, as shown in Figs. 10(a) and 10(d). The *p*-type Seebeck coefficient is more than 1.5 times larger compared to that of the *n*-type system considering the same carrier concentration. Spin-orbit interaction is found to be lower for *p*-type Seebeck coefficients by about 10% on average, while *n*-type Seebeck coefficients are not effected. Since the electrical conductivity (σ) is given as $\sigma = ne\mu$, where n is the carrier concentration, e is the unit charge, and μ is the mobility, we find

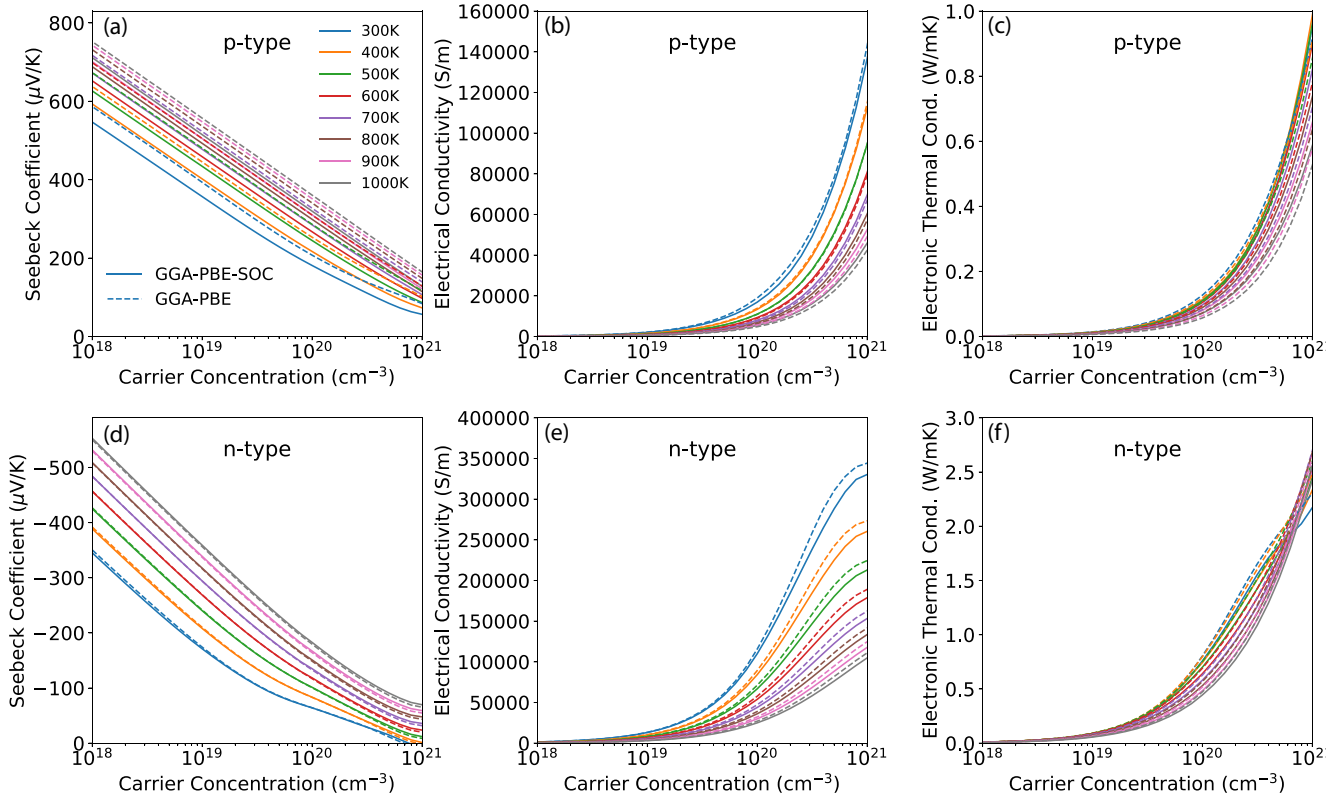

FIG. 10. Electronic transport properties of $BaIn_2Te_4$ calculated with GGA-PBE-SOC (full lines) and GGA-PBE (dashed lines) as a function of carrier concentration with temperatures in the range of 300–1000 K. (a) Seebeck coefficient, (b) electrical conductivity, and (c) electronic thermal conductivity for a *p*-type system; and (d) Seebeck coefficient, (e) electrical conductivity, and (f) electronic thermal conductivity for an *n*-type system.

that electrical conductivity increases with increasing carrier concentration for both types of doping [Figs. 10(b) and 10(e)]. Electrical conductivity decreases with temperature due to the strengthening of scattering mechanisms at high temperatures. The *n*-type electric conductivity is found to be several times larger than that of *p*-type doping. As an example, at 300 K and 10^{20} cm^{-3} carrier concentration, the electrical conductivity of *n*-type doping is about six times larger than that of the *p*-type system. Inclusion of spin-orbit interactions causes a slight decrease in the *n*-type electrical conductivity.

We see from Figs. 10(c) and 10(f) that the electronic thermal conductivity (κ_e) is slightly affected by the inclusion of SOC. κ_e increases with increasing carrier concentration and can reach vaules of 0.5–0.9 (2.3–2.7) W/mK for *p*-type (*n*-type) systems at 10^{21} cm^{-3} carrier concentrations in a 300–1000 K range. Due to the increasing scattering processes at high temperatures, electronic thermal conductivity decreases with increasing temperature. But at higher concentrations, the *p*-type κ_e is at the order of lattice thermal conductivity, and the *n*-type κ_e largely exceeds lattice thermal conductivity. This behavior is unfavorable for high ZT, especially for the *n*-type system.

The power factor ($PF = S^2\sigma$) as a function of carrier concentration given with various temperatures helps us to investigate the optimal doping for a good thermoelectric behavior in the framework of the electronic transport. We present the direction-averaged results in Figs. 11(a) and 11(c) for *p*-type and *n*-type dopings, respectively. The direction-oriented results can be found in Figs. S2a and S2c of the Supplemental Material [45]. The opposite behavior of Seebeck coefficients and electrical conductivity with respect to carrier concentration leads to the higher PF values in moderate concentrations. The highest PF is found at carrier concentrations close to 10^{21} cm^{-3} for *p*-type doping and 10^{20} cm^{-3} for *n*-type doping. The reduction of *p*-type Seebeck coefficients on SOC calculations largely reduces the *p*-type power factors. The decrement of PF caused by SOC is quite small in the *n*-type system as the reduction in electrical conductivity is small. Taking into account SOC results, despite the lower electrical conductivity of *p*-type doping, due to its higher Seebeck coefficient, the PF of the *p*-type system is found to be slightly higher compared to that of the *n*-type system. For the *n*-type system, the increment of the highest PF value with increasing temperature is found to be shortened. Moreover, for the *p*-type system, the highest PF value increases from 300 to 600 K and then starts to decrease due to the decrement of electrical conductivity together with the similar values of high-temperature Seebeck coefficients. For the temperatures between 300 and 1000 K, the PF values are obtained in the range of 0.6−0.9 mW/mK^2 for *p*-type and 0.4−0.8 mW/mK^2 for *n*-type doping. We can conclude that our *p*-type PF highest values are moderate compared to well-known thermoelectric *p*-doped telluride $Sn_{1-x}Mn_xTe$ [60], with the highest PF values obtained around 2 mW/mK^2.

After a detailed investigation of the thermoelectric transport properties, combined with the calculated lattice thermal

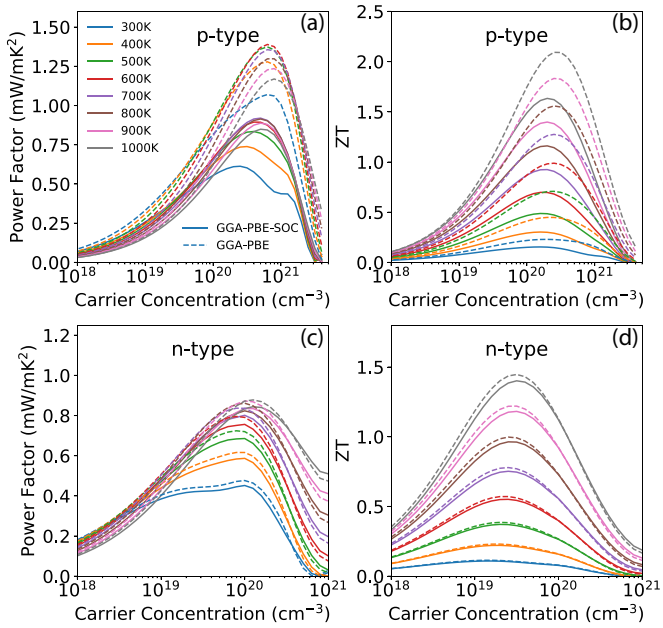

FIG. 11. Power factor and ZT of $BaIn_2Te_4$ calculated with GGA-PBE-SOC (full lines) and GGA-PBE (dashed lines) as a function of carrier concentration with temperatures in the range of 300–1000 K. (a) Power factor and (b) ZT of the p-type system, and (c) power factor and (d) ZT of the n-type system.

conductivity, we predicted the average ZT of $BaIn_2Te_4$ with respect to carrier concentration and temperatures in a range 300–1000 K. The results calculated with GGA-PBE and GGA-PBE-SOC are given in Figs. 11(b) and 11(d) for p-type and n-type dopings, respectively. The direction-oriented results can also be found in Figs. S2b and S2d of the Supplemental Material [45]. Due to the increasing behavior of electronic thermal conductivity with respect to carrier concentration, the highest predicted ZT values are obtained at somewhat lower concentrations compared to the highest PFs. The spin-orbit interactions strongly effect the p-type ZT values. In the framework of SOC included calculations, the highest predicted ZT is calculated to be around 2×10^{20} cm^{-3} for p-type and around 3.2×10^{19} cm^{-3} for n-type systems. In the p-type system, the maximum ZT exceeds unity after 700 K and reaches a value of 1.63 at 1000 K. In the case of n-type doping, the maximum ZT exceeds unity after 800 K and reaches a value of 1.40 at 1000 K. Our p-type predicted ZT value at 900 K is 1.4, which is larger than the experimentally obtained 1.3 value for p-doped $Sn_{1-x}Mn_xTe$ [60] at the same temperature. Together with the moderate PF values of $BaIn_2Te_4$, the predicted high ZT values are achieved because of its low lattice thermal conductivity. By considering the anisotropic behavior of the electronic transport properties (see Fig. S1 of the Supplemental Material [45]) together with the anisotropy of lattice thermal conductivity (Fig. 4), we also predicted higher ZT values along the y-direction with 1.76 for the p-type system, and along the z-direction 1.76 for the n-type system, at 1000 K (see Fig. S2 of the Supplemental Material [45]).

IV. CONCLUSION

The average lattice thermal conductivity values calculated based on the first-principles solution of the linearized phonon Boltzmann transport equation for different temperatures are in very good agreement with the experimentally measured ones. The detailed investigations show that (i) high-negative mode Grüneisen parameters, (ii) extremely low phonon group velocities of particularly acoustic modes, and (iii) high phonon scattering rates at low-frequency regions due to the hybridization of low optical modes with LA modes can be considered as the main sources of the predicted low lattice thermal conductivity. Apart from that, we determined that the semi-one-dimensional chain structure within the crystal has a notable influence on lattice thermal transport and results in highly anisotropic transport properties: the lattice thermal conductivity in the x-direction was found to be approximately 1.7 (1.8) times larger than in the y (z) directions.

The calculated band-gap values with both regular and semicorrected functionals are in sharp contrast with the available measurements, and these results clearly point out the need for further experimental research in that sense. Seebeck coefficients of p-type doped $BaIn_2Te_4$ exhibit much larger values than the n-type material at the same concentration, while the electrical conductivity value of n-type material is found to be much larger than the p-type system. We also report that the spin-orbit coupling effects cannot be ignored for their thermoelectric properties, especially for the p-type system.

More importantly, along with the analysis of the thermoelectric properties, we predict that the orthorhombic $BaIn_2Te_4$ exhibits high ZT values desired for technological applications, and this material can be considered a superior thermoelectric material with both p-type and n-type doping. Note that the highest ZT values are predicted along the off-chain y-direction for p-type doping and the z-direction for n-type doping. This material can be further investigated via spark plasma sintering fabrication and chemical doping to completely evaluate its thermoelectric potential.

ACKNOWLEDGMENTS

C.S. acknowledges the support from the Eskisehir Technical University (ESTU-BAP 22ADP150). The numerical calculations reported in this paper were partially performed at TUBITAK ULAKBIM, High Performance and Grid Computing Center (TRUBA resources).

[1] I. T. Witting, T. C. Chasapis, F. Ricci, M. Peters, N. A. Heinz, G. Hautier, and G. J. Snyder, Adv. Electron. Mater. **5**, 1800904 (2019).

[2] J. P. Heremans, V. Jovovic, E. S. Toberer, A. Saramat, K. Kurosaki, A. Charoenphakdee, S. Yamanaka, and G. J. Snyder, Science **321**, 554 (2008).

[3] Y. Pei, A. LaLonde, S. Iwanaga, and G. J. Snyder, Energy Environ. Sci. **4**, 2085 (2011).

[4] A. Yusufu, K. Kurosaki, A. Kosuga, T. Sugahara, Y. Ohishi, H. Muta, and S. Yamanaka, Appl. Phys. Lett. **99**, 061902 (2011).

[5] T. Plirdpring, K. Kurosaki, A. Kosuga, T. Day, S. Firdosy, V. Ravi, G. J. Snyder, A. Harnwunggmoung, T. Sugahara, Y. Ohishi *et al.*, Adv. Mater. **24**, 3622 (2012).

[6] Y. Luo, J. Yang, Q. Jiang, W. Li, D. Zhang, Z. Zhou, Y. Cheng, Y. Ren, and X. He, Adv. Energy Mater. **6**, 1600007 (2016).

[7] H. Xie, S. Hao, T. P. Bailey, S. Cai, Y. Zhang, T. J. Slade, G. J. Snyder, V. P. Dravid, C. Uher, C. Wolverton *et al.*, J. Am. Chem. Soc. **143**, 5978 (2021).

[8] J. W. Sharp, B. C. Sales, D. G. Mandrus, and B. C. Chakoumakos, Appl. Phys. Lett. **74**, 3794 (1999).

[9] B. Wölfing, C. Kloc, J. Teubner, and E. Bucher, Phys. Rev. Lett. **86**, 4350 (2001).

[10] K. Kurosaki, A. Kosuga, and S. Yamanaka, J. Alloys Compd. **351**, 279 (2003).

[11] M. K. Jana, K. Pal, A. Warankar, P. Mandal, U. V. Waghmare, and K. Biswas, J. Am. Chem. Soc. **139**, 4350 (2017).

[12] D.-Y. Chung, T. Hogan, P. Brazis, M. Rocci-Lane, C. Kannewurf, M. Bastea, C. Uher, and M. G. Kanatzidis, Science **287**, 1024 (2000).

[13] A. Assoud, S. Derakhshan, N. Soheilnia, and H. Kleinke, Chem. Mater. **16**, 4193 (2004).

[14] Z. Ma, T. Xu, W. Li, Y. Cheng, J. Li, D. Zhang, Q. Jiang, Y. Luo, and J. Yang, Adv. Funct. Mater. **31**, 2103197 (2021).

[15] G. J. Snyder and E. S. Toberer, Nat. Mater. **7**, 105 (2008).

[16] G. Nolas, D. Morelli, and T. M. Tritt, Annu. Rev. Mater. Sci. **29**, 89 (1999).

[17] M. Rull-Bravo, A. Moure, J. F. Fernández, and M. Martín-González, RSC Adv. **5**, 41653 (2015).

[18] T. Takabatake, K. Suekuni, T. Nakayama, and E. Kaneshita, Rev. Mod. Phys. **86**, 669 (2014).

[19] J. Shuai, J. Mao, S. Song, Q. Zhang, G. Chen, and Z. Ren, Mater. Today Phys. **1**, 74 (2017).

[20] E. S. Toberer, A. F. May, and G. J. Snyder, Chem. Mater. **22**, 624 (2010).

[21] G. A. Slack, *CRC Handbook of Thermoelectrics* (CRC, Boca Raton, FL, 1995).

[22] E. R. Franke and H. Schäfer, Z. Naturforsch. B **27**, 1308 (1972).

[23] P. Dotzel, E. Franke, H. Schäfer, and G. Schön, Z. Naturforsch. B **30**, 179 (1975).

[24] W. Klee and H. Schäfer, Z. Anorg. Allg. Chem. **479**, 125 (1981).

[25] S.-J. Kim, S. Hu, C. Uher, and M. G. Kanatzidis, Chem. Mater. **11**, 3154 (1999).

[26] J. H. Kim and J.-S. Rhyee, Electr. Mater. Lett. **10**, 801 (2014).

[27] M. Ishtiyak, S. Jana, S. Narayanswamy, A. K. Nishad, G. Panigrahi, P. P. Bhattacharjee, and J. Prakash, J. Alloys Compd. **802**, 385 (2019).

[28] M. Sun, X. Zhang, W. Xing, Z. Li, W. Liu, Z. Lin, W. Yin, and J. Yao, Inorg. Chem. **60**, 14793 (2021).

[29] M. Rashid, A. S. Alghamdi, Q. Mahmood, M. Hassan, M. Yaseen, and A. Laref, Phys. Scr. **94**, 125709 (2019).

[30] H. Liu, X. Yu, K. Wu, Y. Gao, S. Tongay, A. Javey, L. Chen, J. Hong, and J. Wu, Nano Lett. **20**, 5221 (2020).

[31] Z. Zeng, C. Zhang, N. Ouyang, and Y. Chen, Phys. Rev. B **106**, 054302 (2022).

[32] J. Zhang, D. He, H. Jiang, X. Xia, Y. Gao, and Z. Huang, ACS Appl. Energy Mater. **5**, 5146 (2022).

[33] G. Kresse and J. Furthmüller, Phys. Rev. B **54**, 11169 (1996).

[34] P. Hohenberg and W. Kohn, Phys. Rev. **136**, B864 (1964).

[35] W. Kohn and L. J. Sham, Phys. Rev. **140**, A1133 (1965).

[36] G. Kresse and D. Joubert, Phys. Rev. B **59**, 1758 (1999).

[37] J. P. Perdew, K. Burke, and M. Ernzerhof, Phys. Rev. Lett. **77**, 3865 (1996).

[38] A. V. Krukau, O. A. Vydrov, A. F. Izmaylov, and G. E. Scuseria, J. Chem. Phys. **125**, 224106 (2006).

[39] A. Togo and I. Tanaka, Scr. Mater. **108**, 1 (2015).

[40] W. Li, J. Carrete, N. A. Katcho, and N. Mingo, Comput. Phys. Commun. **185**, 1747 (2014).

[41] A. M. Ganose, J. Park, A. Faghaninia, R. Woods-Robinson, K. A. Persson, and A. Jain, Nat. Commun. **12**, 2222 (2021).

[42] G. K. Madsen and D. J. Singh, Comput. Phys. Commun. **175**, 67 (2006).

[43] G. K. Madsen, J. Carrete, and M. J. Verstraete, Comput. Phys. Commun. **231**, 140 (2018).

[44] S. Baroni, S. de Gironcoli, A. Dal Corso, and P. Giannozzi, Rev. Mod. Phys. **73**, 515 (2001).

[45] See Supplemental Material at http://link.aps.org/supplemental/10.1103/PhysRevB.106.195204 for (i) bulk modulus equation of state, (ii) basis vectors of the crystal, (iii) parameters used in AMSET calculations, and (iv) direction-oriented thermoelectric properties.

[46] D. Hicks, M. J. Mehl, E. Gossett, C. Toher, O. Levy, R. M. Hanson, G. Hart, and S. Curtarolo, Comput. Mater. Sci. **161**, S1 (2019).

[47] K. Momma and F. Izumi, J. Appl. Crystallogr. **44**, 1272 (2011).

[48] M. Hebbache and M. Zemzemi, Phys. Rev. B **70**, 224107 (2004).

[49] S. Kumar, N. Kumar, K. Yadav, A. Kumar, and R. Singh, Optik **207**, 163797 (2020).

[50] B. Bahloul, A. Bentabet, L. Amirouche, Y. Bouhadda, S. Bounab, B. Deghfel, and N. Fenineche, J. Phys. Chem. Solids **75**, 307 (2014).

[51] Z. Tian, J. Garg, K. Esfarjani, T. Shiga, J. Shiomi, and G. Chen, Phys. Rev. B **85**, 184303 (2012).

[52] H. Zhu, R. He, J. Mao, Q. Zhu, C. Li, J. Sun, W. Ren, Y. Wang, Z. Liu, Z. Tang *et al.*, Nat. Commun. **9**, 1 (2018).

[53] J. Cao, J. D. Querales-Flores, A. R. Murphy, S. Fahy, and I. Savić, Phys. Rev. B **98**, 205202 (2018).

[54] Z. Li, X. Su, and X. Tang, ACS Appl. Mater. Interfaces **14**, 6916 (2022).

[55] J. Ma, Y. Chen, and W. Li, Phys. Rev. B **97**, 205207 (2018).

[56] W. Rahim, J. M. Skelton, and D. O. Scanlon, J. Mater. Chem. A **9**, 20417 (2021).

[57] J.-H. Pöhls, S. Chanakian, J. Park, A. M. Ganose, A. Dunn, N. Friesen, A. Bhattacharya, B. Hogan, S. Bux, A. Jain *et al.*, Mater. Horiz. **8**, 209 (2021).

[58] Z. Li, H. Xie, Y. Xia, S. Hao, K. Pal, M. G. Kanatzidis, C. Wolverton, and X. Tang, Chem. Mater. **34**, 1289 (2022).

[59] Y.-K. Jung, I. T. Han, Y. C. Kim, and A. Walsh, npj Comput. Mater. **7**, 1 (2021).

[60] G. Tan, F. Shi, S. Hao, H. Chi, T. P. Bailey, L.-D. Zhao, C. Uher, C. Wolverton, V. P. Dravid, and M. G. Kanatzidis, J. Am. Chem. Soc. **137**, 11507 (2015).